Antiferromagnetic math xmlns="http://www.w3.org/1998/Math/MathML">mrow>mi>Fe/mi>msub>mi>Te/mi>mn>2/mn>/msub>/mrow>mo>/mo>mrow>mn>1/mn>mi>T/mi>mtext>−/mtext>mi>phase/mi>/mrow>/math> formation at the math xmlns="http://www.w3.org/1998/Math/MathML">mrow>msub>mi>Sb/mi>mn>2/mn>/msub>msub>mi>Te/mi>mn>3/mn>/msub>mo>//mo>msub>mi>Ni/mi>mn>80/mn>/msub>msub>mi>Fe/mi>mn>20/mn>/msub>/mrow>/math> interface

A. R. Will-Cole, James L. Hart, Matthew Matzelle, Adrian Podpirka, Nirjhar Bhattacharjee, Shreya K. Patel, Sarah H. Tolbert, Arun Bansil, Judy J. Cha, Don Heiman, and Nian X. Sun

Phys. Rev. Materials **7**, 024406 — Published 15 February 2023

DOI: 10.1103/PhysRevMaterials.7.024406

Antiferromagnetic $FeTe_2$ 1T-Phase Formation at the $Sb_2Te_3/Ni_{80}Fe_{20}$ Interface

A.R. Will-Cole,[1] James L. Hart,[2] Matthew Matzelle,[3] Adrian Podpirka,[4] Nirjhar Bhattacharjee,[1] Shreya K. Patel,[5] Sarah H. Tolbert,[5] Arun Bansil,[3] Judy J. Cha,[2] Don Heiman,[3,6] and Nian X. Sun[1]

[1]*Electrical and Computer Engineering, Northeastern University, Boston, 02115, USA*
[2]*Materials Science and Engineering, Cornell University, Ithaca, 14853, USA*
[3]*Physics, Northeastern University, Boston, 02115, USA*
[4] *Applied Physics Laboratory, Johns Hopkins, Laurel, 20723, USA*
[5]*Chemistry, University of California Los Angeles, Los Angeles, 90095, USA*
[6]*Plasma Science and Fusion Center, Massachusetts Institute of Technology, Cambridge, 02139, USA*

Abstract

Bilayer topological insulator/ferromagnet (TI/FM) heterostructures are promising for spintronic applications due to their low switching energy and therefore power efficiency. Until recently, the reactivity of TI with FM films was overlooked in the spin-orbit-torque literature, even though there are reports that it is energetically favorable for TIs to react with transition metals and form interfacial layers. In this study we fabricated a TI/FM heterostructure comprised of molecular beam epitaxy grown Sb_2Te_3 and DC sputtered $Ni_{80}Fe_{20}$. Broadband ferromagnetic resonance revealed spin-pumping evident by the significant enhancement in Gilbert damping, which is likely a signature of the topological surface states or the presence of large spin-orbit-coupling in the adjacent Sb_2Te_3. With low-temperature magnetometry, an exchange bias is observed which indicates an exchange interaction between an antiferromagnet (AFM) and an adjacent FM. Cross-section high-angle annular dark field scanning transmission electron microscopy (HAADF-STEM) characterization of the Sb_2Te_3 - $Ni_{80}Fe_{20}$ bilayer revealed a complex interface showing diffusion of Fe and Ni into the Sb_2Te_3 film yielding the formation of a $FeTe_2$-1T type structural phase. Furthermore, density functional theory calculations revealed that the $FeTe_2$ 1T-phase has an AFM ground state. Due to experimental limitations in the electron energy loss spectroscopy measurements precise chemistry of the interfacial phase could not be determined, therefore it is possible that the $FeTe_2$-1T and/or an intermixed $(Fe_{1-x}Ni_x)Te_2$-1T is the AFM interfacial phase contributing to exchange bias in the system. This work emphasizes the chemical complexity of TI/FM interfaces that host novel, metastable magnetic topological phases and require more in-depth studies of other similar interfaces.

Keywords: Topological Insulators; Antiferromagnet; Thin Film Interfaces;

Introduction

Topological insulators (TIs), specifically $Bi_{1-x}Sb_x$ alloys and Van der Waals (VdW) chalcogenides X_2Q_3 (X = Bi, Sb, $Bi_{1-x}Sb_x$; Q = Se, Te) with tetradymite structure, have insulating bulk state and two-dimensional metallic surfaces enabled by topologically protected Dirac surface states.[1-3] TIs exhibit large charge-to-spin conversion efficiencies, strong spin-momentum locking, and conductive surface states making them ideal for applications in spin-orbit-torque magnetic random access memory (SOT-MRAM) magnetic tunnel junction devices.[4-10] When magnetic order is introduced, time-reversal symmetry is broken, providing an energy gap in the surface states, and the electrons gain a net moment through short-range exchange interactions.[11] Magnetic TIs can exhibit exciting behavior such as anomalous Hall effect, quantum anomalous Hall effect, axion insulator and topological magnetoelectric effect.[11-13] Strategies to achieve magnetic order in TI include compositional doping, intrinsic magnetic TI, or proximity-induced magnetization (PIM).[14-18] PIM can be achieved through growing magnetic insulator (MI) films directly on the TI surface.[17-21]

For spin-orbit-torque devices based on TIs coupled with ferromagnets (FMs), there remains integration feasibility considerations such as interfacial orbital hybridization, novel interfacial chemical phases, etc. However, this is often

overlooked or not mentioned in literature on spin-pumping in these TI/metallic FM heterostructures.[9,22,23] There have been theoretical studies on the interface between TIs and metal contacts, namely Au/Bi_2Se_3 and graphene/Bi_2Se_3 that retain spin-momentum locking of the surface states, while Pd and Pt strongly couple to Bi_2Se_3 and cause delocalization of the surface states and less efficient spin-momentum locking.[24] Additionally, experiments confirm, band bending occurs at the Bi_2Se_3/metallic interface due to variation in electron affinity of Bi_2Se_3 (4.45 eV) and work functions of transition metal contacts (~5 eV).[25] The formation of interfacial layers in Bi_2Se_3/metal contacts and Bi_2Se_3/magnetic materials has been confirmed with X-ray photoelectron spectroscopy, and aside from Au that was found inert, the metals were ranked by reaction strength (determined by the amount of Bi_2Se_3 consumed) as follows: Pd < Ir < Co < CoFe < Ni < Cr < NiFe < Fe.[26]

More recently, novel materials have been found at the interfaces in TI/FM structures generated by interdiffusion and subsequent reactions. Ni diffusion in $Ni_{80}Fe_{20}/Bi_2Se_3$ heterostructures resulted in a ternary magnetic phase of Ni:Bi_2Se_3.[27] Further study of $Bi_2Te_3/Ni_{80}Fe_{20}$ interface resulted in the discovery of the intrinsic antiferromagnetic (AFM) $NiBi_2Te_4$.[28] This unique material has a Néel temperature of T_N=63 K that is significantly higher than that reported for intrinsic antiferromagnetic topological insulator,[28] $MnBi_2Te_4$, which has T_N=25 K.[16] The discovery of $NiBi_2Te_4$ at the interface of $Bi_2Te_3/Ni_{80}Fe_{20}$ revealed that novel magnetic topological phases can exist at the interfaces and thus these reactive TI interfaces can be used as a test bed for stable and metastable quantum materials discovery.[28]

The goal of our study is to investigate the TI/FM heterostructure and interface of $Sb_2Te_3/Ni_{80}Fe_{20}$, where the Sb_2Te_3 is epitaxially grown by molecular beam epitaxy (MBE) on GaAs substrate. The FM, $Ni_{80}Fe_{20}$ is sputter deposited on the Sb_2Te_3 film. We provide evidence that a novel AFM phase forms at the interface which is structurally consistent with $FeTe_2$ 1T-phase (similar to the $NiTe_2$-type structure, specifically $P\bar{3}m1$). Additionally, our theoretical calculations indicate that the $FeTe_2$ 1T-phase has an AFM ground state, which is supported by an exchange bias observed in our magnetometry measurements. This $FeTe_2$ phase is a magnetic transition metal dichalcogenide (TMD) with the chemical structure XY_2 comprised of transition metal and chalcogen elements (X=Fe, Ni, W, Pd etc., Y=S, Se, Te, etc.) – these materials have been extensively studied since TMDs were proposed to host type-II Dirac fermions.[29,30] Experimentally, there have been two recent studies on the $FeTe_2$ 1T-phase – this phase has been stabilized in the form of nanoflakes via chemical vapor deposition,[31] and in the form of single crystals.[32] Neither of these studies explicitly report the presence of AFM order, however in the single crystal investigation an isostructural transition was observed with X-ray diffraction accompanied by a sharp decrease in magnetization which was attributed to the presence of AFM coupling.[32]

Experimental Results & Discussion

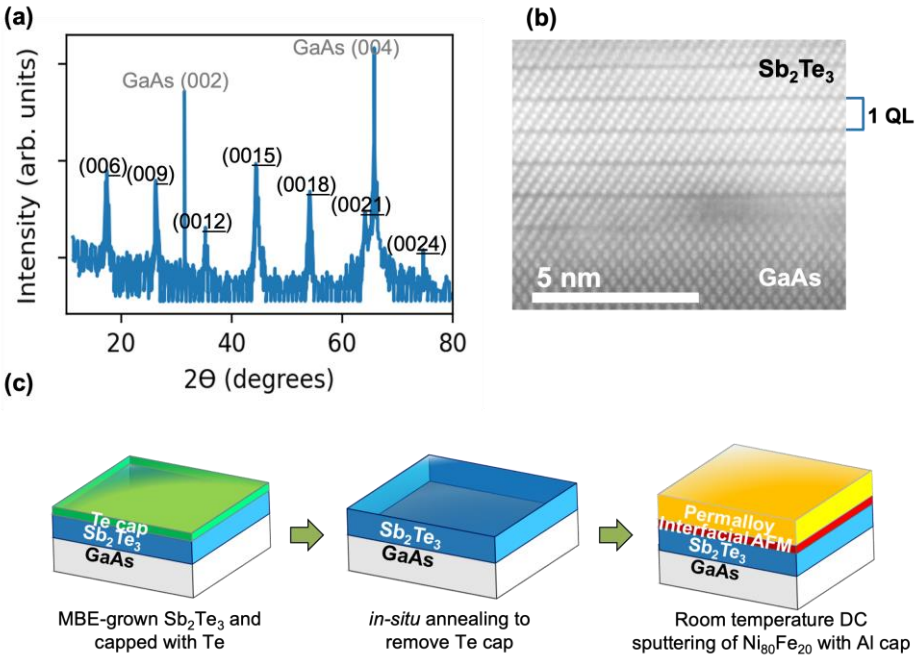

FIG 1. (a) X-ray diffraction spectra of Sb_2Te_3/GaAs with labeled diffraction peaks. Grey font labelled peaks correspond to the GaAs substrate and black font labelled peaks correspond to the Sb_2Te_3 film. (b) High-angle annular dark-field scanning transmission electron microscopy cross-section image with GaAs and Sb_2Te_3 in view. The quintuple layer Van der Waals structure is highlighted with each quintuple layer corresponding to approximately 1 nm thick. (c) The fabrication process flow is highlighted here, specifically the MBE growth of TI, Te-cap removal, and magnetic film deposition.

In this study we fabricated a Sb_2Te_3/ $Ni_{80}Fe_{20}$ bilayer heterostructure on a GaAs substrate via a combinational growth regime. First, a 10 nm thick Sb_2Te_3 was epitaxially grown with molecular beam epitaxy (MBE) on a GaAs (100)-oriented substrate and capped with Te.[33] To confirm the crystalline quality of the Sb_2Te_3 film, high-angle, out-of-plane X-ray diffraction (XRD) was performed. The XRD pattern for the Sb_2Te_3 sample shown in Figure 1(a) demonstrates the anticipated tetradymite crystal structure. The XRD pattern confirms a highly *c*-axis oriented growth of the TI film as evident by the presence of (00*l*)-peaks in the diffraction pattern. The rocking curve can be found in S1 of the Supplemental Material and shows that MBE-grown TI on a lattice matched substrate has higher crystal quality than comparable sputtered TI on an amorphous substrate.[28,34] Additionally, cross-section high-angle annular dark field scanning transmission electron microscopy (HAADF-STEM) imaging revealed further evidence of the VdW structure of the Sb_2Te_3 film – shown in Figure 1(b). The TI growth on the GaAs (100)-oriented substrate is slightly disordered for the first quintuple layer, likely due to the symmetry mismatch of the film to the substrate. However, by the second quintuple layer the anticipated VdW tetradymite crystal structure can be seen for the Sb_2Te_3 film. Subsequent to the MBE-growth of Sb_2Te_3 vacuum was broken and the films were transferred into the sputtering chamber. The Te cap was removed with an *in-situ* sublimation process consistent with methods established in the literature.[35] After cooling the sample to room temperature and achieving a base vacuum of less than $1.0x10^{-7}$ Torr, a 15 nm $Ni_{80}Fe_{20}$ (also known as permalloy, referred to as Py in the rest of the text and upcoming figures) film was DC sputtered at a power of 50 W. This was followed by a DC sputtered Al-cap of 2 nm on the film surface to prevent undesirable oxidation of the magnetic film. The fabrication process flow is provided in Figure 1(c).

We performed room temperature broadband ferromagnetic resonance (FMR) spectroscopy to confirm spin-pumping in the Sb_2Te_3/Py heterostructure samples. In the broadband FMR measurement at resonance, the Py magnetization precession acts as a source of angular momentum, and since Sb_2Te_3 acts as a spin sink due to its large spin-orbit-coupling and/or the presence of topologically-protected surface states (TSS), this leads to spin pumping (generation of spin current) across the interface into the Sb_2Te_3 layer – a schematic of the spin-pumping phenomenon is provided in Figure 2(a). Therefore, there is a loss in angular momentum in the Py due to spin pumping across the interface. Spin pumping results in a significant enhancement in the Gilbert damping parameter, α, in the Sb_2Te_3/Py samples compared to a control sample of Py. Magnetic field sweep FMR measurements of Sb_2Te_3/Py and a control sample of Si/Al/Py/Al yielded the differential absorption spectra at each frequency (f) and only one derivative peak was observed which is the main resonance uniform mode. The Gilbert damping constant was extracted from a linear fit to the $\Delta H/\Delta f$ as a function of frequency using the relation provided in Eq. (1), where ΔH_{FWHM} is the uniform mode linewidth, ΔH_0 is the inhomogeneous linewidth broadening, and γ is the gyromagnetic ratio (2.8 MHz/Oe for magnetic films).[36]

$$\Delta H_{FWHM} = \Delta H_0 + \frac{2\pi\alpha}{\gamma} \tag{1}$$

The FMR results for Sb_2Te_3/Py and Si/Al/Py/Al are shown in Figure 2(b), and the extracted α damping parameter is shown in Table I. As shown in Table I, there is giant enhancement in the Gilbert damping for the Sb_2Te_3/Py bilayer (an order of magnitude higher than the Si/Al/Py/Al control sample). This can be attributed to the TSS or presence of

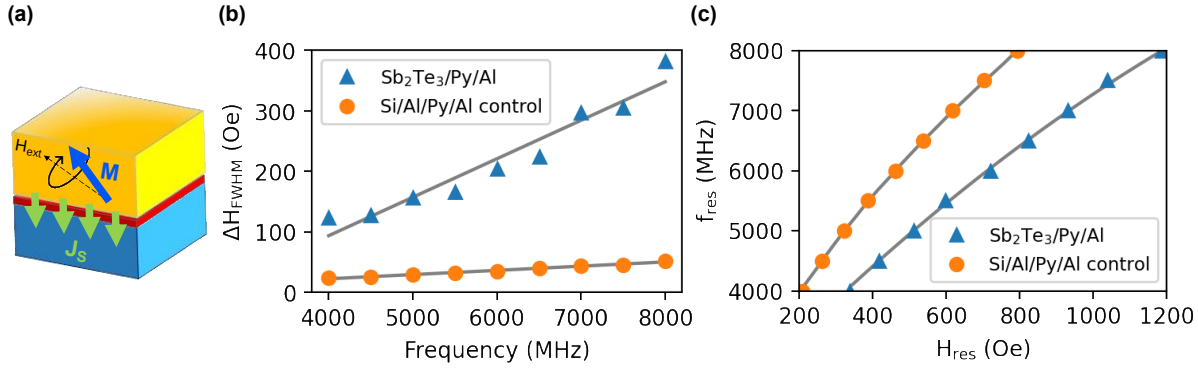

FIG 2. (a) Schematic of spin-pumping. (b) Uniform mode resonance linewidth versus frequency with linear fit described by Eq. (1) to extract the Gilbert damping constant. (c) Frequency versus uniform mode resonance field with Kittel fit to extract effective in-plane magnetization.

large spin-orbit-coupling in the Sb_2Te_3 layer (likely the later as the Sb_2Te_3 bulk conduction channels are not suppressed).[37-40] The effective in-plane magnetization, $4\pi M_{eff}$, was further extracted using the Kittel equation provided in Eq. (2), where H_{RES} is the resonance field, and γ is the gyromagnetic ratio (2.8 MHz/Oe for magnetic materials).

$$f = |\gamma/2\pi|\sqrt{H_{RES}(H_{RES} + 4\pi M_{eff})} \quad (2)$$

The results are shown in Figure 2(c), and the extracted $4\pi M_{eff}$ is shown in Table I. There is a reduction in the $4\pi M_{eff}$ between the Si/Al/Py/Al control and the Sb_2Te_3/Py heterostructure, which likely indicates out-of-plane canting leading to an out-of-plane magnetic component in the Py film or a reduction in magnetization of the FM film (this result is directly compared to the hysteresis loops in S2 of the Supplemental Material).[34] Regardless, the Gilbert damping enhancement is indicative of spin-pumping in the Sb_2Te_3/Py bilayer system.

TABLE I: Broadband FMR measurement results

	α	$4\pi M_{eff}$
Si/Al/Py/Al	0.019	9.54 kG
Sb_2Te_3/Py	0.178	5.77 kG

The reduction in $4\pi M_{eff}$ between the Si/Al/Py/Al control and the Sb_2Te_3/Py heterostructure may indicate there is a reduction in magnetization rather than just the possibility of out-of-plane canting, so to further study the magnetic phases present, we measured the static, in-plane magnetic properties for the Sb_2Te_3/Py heterostructure as a function of decreasing temperature using a superconducting quantum interference device (SQUID) magnetometer. Magnetic hysteresis loop measurements revealed a large exchange bias (H_{EB} ~ 100 Oe) present at low temperature (T = 6 K) with +1 T and -1 T field cooling as shown in Figure 3(a) compared with the room temperature (T = 300 K) hysteresis loop. The exchange bias effect is observed in coupled FM/AFM materials and arises due to uniaxial magnetic anisotropy induced at the interface between the two layers.[41] Our Figure 3 suggests FM/AFM coupling is present here, and since the Sb_2Te_3 is non-magnetic and the Py film is FM, we conclude there is an interfacial AFM layer between Sb_2Te_3 and Py. In addition to the presence of the large exchange bias, we observe an accompanying increase in the Py coercive field, H_C, from ~4.25 Oe at T = 300 K to ~113.5 Oe (~94 Oe) at T = 6 K for 1 T (-1 T) field cooling condition. The exchange interaction between FM and AFM not only causes exchange bias, but also leads to a significant increase in coercive field possibly due to domains at a magnetically frustrated interface.[28] We also explored the magnitude of the exchange bias effect as a function of different field cooling conditions, which is displayed in Figure 3(b) – we observe a negative exchange bias effect, such that the hysteresis loops are shifted oppositely to the applied field cooling direction. Temperature resolved magnetometry was used to identify the Néel transition temperature (T_N) for the AFM. The magnetic moment was measured as a function of temperature with +1 T field cooling and zero field cooling for the Sb_2Te_3/Py heterostructure as shown in Figure 3(c). The derivative of the moment with respect to the temperature is taken, to identify the Néel temperature, and shown in Figure 3(d). The Néel temperature is found to be T_N = 40 K –

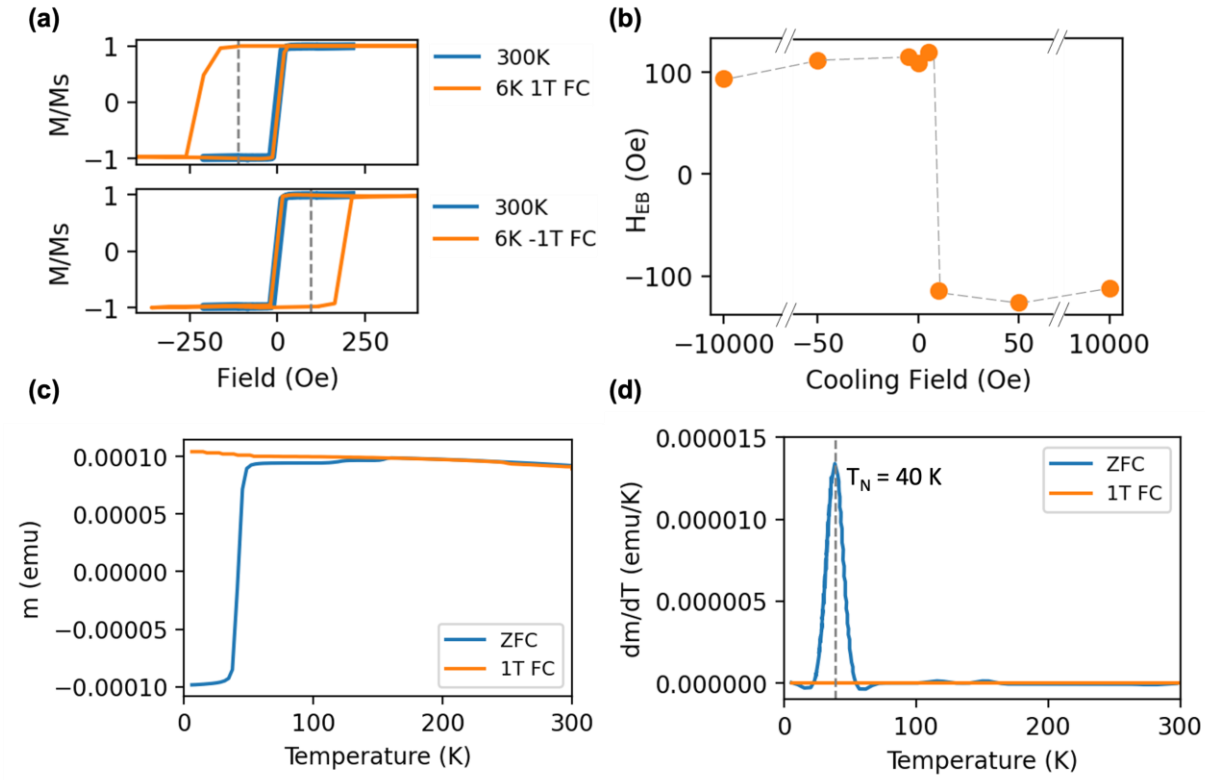

FIG 3. (a) Magnetic hysteresis loop at 300 K and 6 K for Sb_2Te_3/Py with +1 T field cooling (top) and 300 K and 6 K for Sb_2Te_3/Py with -1 T field cooling (bottom). The grey dashed line represents the exchange bias field H_{EB}. (b) The H_{EB} plotted as a function of field cooling condition. (c) Moment as a function of temperature for +1 T field cooled (FC) in orange and zero field cooled (ZFC) in blue. (d) Derivative of moment with respect to temperature for +1 T field cooled (FC) in orange and ZFC in blue. The grey dashed line is simply to highlight the Néel temperature, T_N = 40 K.

this is significantly higher than the most well studied intrinsic topological antiferromagnet, $MnBi_2Te_4$, with T_N ~20-25 K.[16,42] However, it is lower than T_N = 63 K for recently discovered $NiBi_2Te_4$ at a Bi_2Te_3/Py interface.[28] Finally, to confirm the T_N = 40 K corresponds to the onset of exchange bias in the Sb_2Te_3/Py heterostructure, temperature dependent $m(H)$ hysteresis loops were measured between 6 K and 50 K. As shown in Figure 4(a), the exchange bias effect is no longer observed by 50 K as evident by a centered, magnetic hysteresis loop with a narrow H_C. At 40 K, we observe a shift in the magnetic hysteresis loop indicative of a finite exchange bias. Additionally, below 40 K the H_C dramatically increases which also supports the presence of exchange coupling and/or magnetic frustration, i.e., pinned domains. As temperature decreases, the H_{EB} and H_C both increase as summarized in Figure 4(b) and 4(c), respectively. This giant H_C enhancement and presence of H_{EB} disappears at, or close to, the experimentally identified AFM Néel temperature, thus the interfacial AFM phase is responsible for this observed magnetic anisotropy.[40] The observed exchange bias was completely suppressed with the implementation of Te spacer layer (data found in S3 of the Supplemental Material).[34] Therefore, the Te alone is not reactive enough to form the interfacial AFM phase with Py unlike the Sb_2Te_3/Py interface presented here. Besides the presence of exchange bias, there is evidence of magnetic frustration in the system. The irreversibility/bifurcation of the FC/ZFC curves in Figure 3(c) at around 100 K may indicate there is some additional magnetic frustration at the interface. The accompanying exponential decay of the

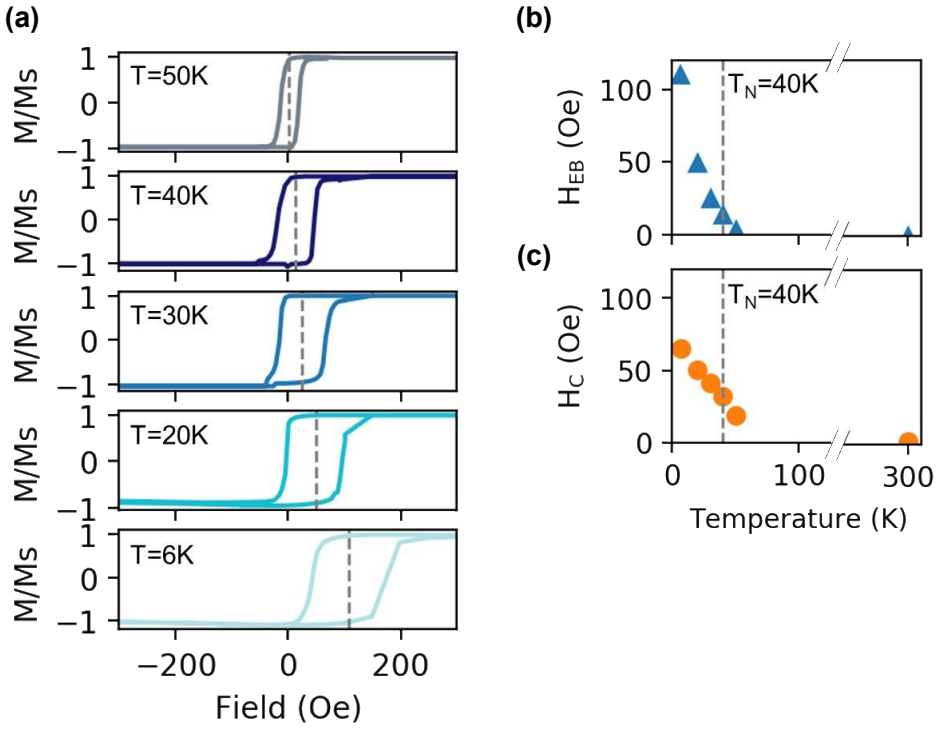

FIG 4. (a) Magnetic hysteresis loop at 50 K, 40 K, 30 K, 20 K and 10 K for Sb_2Te_3/Py with -1 T field cooling. (b) The exchange bias H_{EB} plotted as a function of temperature. (c) The coercive field plotted as a function of temperature.

coercivity with temperature shown in Figure 4(c) may also point to magnetic frustration. The observed signatures of this magnetic frustration may arise due to additional disorder at the interface.

The observed exchange bias in the Sb_2Te_3/Py system is due to an interfacial AFM phase at the interface, analogous to what was reported in the Bi_2Te_3/Py system with an interfacial topological AFM $NiBi_2Te_4$ phase.[28] To investigate the accurate morphology and composition of the interfacial AFM phase, we performed cross-section HAADF-STEM. Focused ion beam (FIB) milling was used to make the cross-section sample and the FIB lift-out had a surface normal of GaAs [011]. As shown in Figure 5(a), the interface between Sb_2Te_3 and Py is complex and disordered, with a high concentration of defects and nanoscale crystalline structures distinct from the Sb_2Te_3 tetradymite structure. The interfacial reaction has partially consumed the Sb_2Te_3 film and has resulted in thickness variation of the Sb_2Te_3 (5-7 QLs) across the heterostructure. The predominant interfacial structure has an out-of-plane lattice constant of 0.5 nm, roughly half that of the Sb_2Te_3 QL. Electron energy loss spectroscopy (EELS) was performed at different sections through the thickness of the heterostructure. The EELS spectra are shown in Figure 5(b). Note there is oxidation

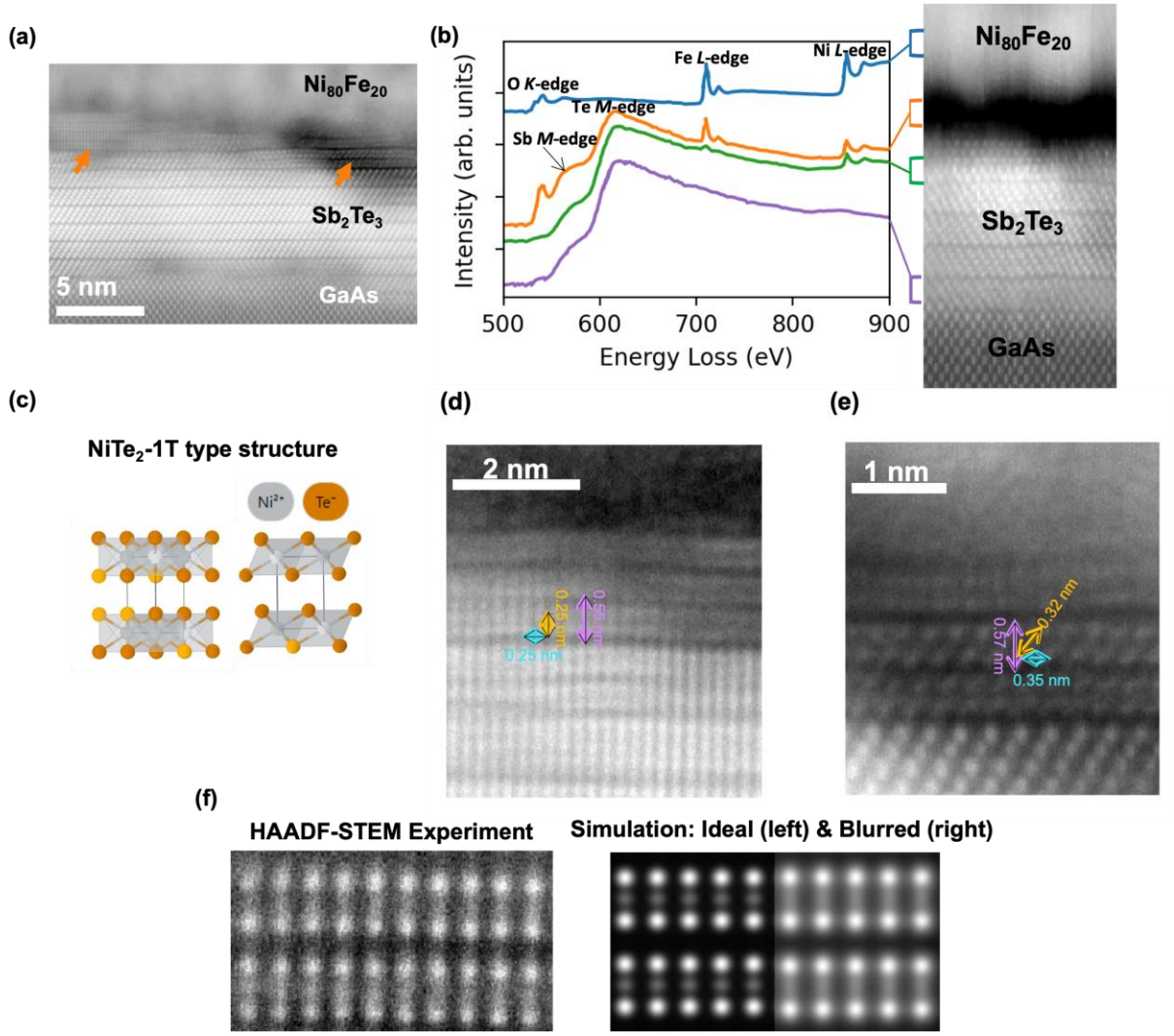

FIG 5. (a) Representative HAADF-STEM cross-section image. Orange arrows point to the interfacial phase. (b) Representative STEM EELS spectra with corresponding STEM image. The colors and lines are a guide to where in the cross-section the data was collected. (c) Atomic models of the $NiTe_2$-type structure in the two common orientations observed at the interface. The structure was retrieved from the Materials Project for $NiTe_2$ (mp-2578) ($P\bar{3}m1$) from database version v2021.11.10. (d) Zoomed-in HAADF-STEM cross-section image of the orientation on the left in (c). (e) Zoomed-in HAADF-STEM cross-section image of the orientation on the right in (c). (f) Experimental HAADF-STEM image of the interfacial $NiTe_2$-type structure (zoomed-in further than (d)). (g) Simulated HAADF-STEM image using COMPUTEM package with and without blurring (right and left, respectively).

present in the sample based on the prevalence of the oxygen *K*-edge which is attributed to the fact that the sample was stored in atmosphere post-FIB lift-out. The presence of the Fe-*L* edge and Ni-*L* edge in the disordered interfacial region (orange) and ordered interfacial phase region (green) indicate that there is diffusion of Fe and Ni into the Sb_2Te_3 film during the room temperature sputter deposition of the Py film. This diffusion is followed by interfacial reaction resulting in an interfacial phase seen in Sb_2Te_3/Py, promoted by the TSS electrons on the Sb_2Te_3 surface. The interfacial phase is consistent with a $NiTe_2$-type structure, specifically $P\bar{3}m1$ (structure retrieved from the Materials Project for $NiTe_2$ (mp-2578) from database version v2021.11.10).[43] For the orientation that is shown in Figure 5(d), the out-of-plane layer spacing is 0.55 nm, the in-plane bond distance is 0.2 nm, the out-of-plane bond distance is 0.25 nm, and the bond angle is 90°. For the orientation shown in Figure 5(e), the out-of-plane layer spacing is 0.57 nm, the in-plane bond distance is 0.35 nm, the out-of-plane bond distance is 0.32 nm, and the bond angle is 55° (estimated error in the bond lengths is 0.03nm). It is important to note that in HAADF-STEM imaging heavier elements correspond to higher intensity, therefore in the images shown in Figure 5 the bright atoms correspond to the Te-sites. Shown in Figure 5(f) is the $NiTe_2$-type interfacial structure with both the Ni- and Te-sites resolved in the image. This HAADF-STEM image was compared to a simulated HAADF-STEM image for the $NiTe_2$), which appears to be visually and qualitatively consistent.[43] The simulated HAADF-STEM image (shown in Figure 5(g)) was generated using Earl Kirkland's COMPUTEM package.[44] There are more STEM images in S4 of the Supplemental Material – these include other instances of the $NiTe_2$-1T like structure and other indications of disorder, specifically stacking fault defects near the interface. We note that the in-plane size of the interfacial domains (<10 nm) is significantly less than the thickness of the STEM specimen. Thus, when the STEM probe is placed over the crystalline interfacial phase shown Figure (5), the probe is likely also passing through the amorphous Py and/or another disordered phase. Thus, we cannot determine the composition of the interfacial $NiTe_2$- like phase, but we note that the Ni, Fe, Te, and Sb are all detected within this region, thus possibly present within this interfacial phase with $NiTe_2$-1T like structure. Therefore, we pursued theoretical calculations to better understand what possible compositions contribute to the AFM-phase.

Theoretical Results & Discussion

Following the experimental results, density functional theory calculations were required to definitively identify the AFM interfacial phase. The magnetometry data and the presence of exchange bias in the heterostructure strongly suggests that there should be an AFM phase in contact with the FM Py at the Sb_2Te_3/Py interface. Based on the STEM-EELS data there is Fe and Ni diffusion in the interfacial phase region, therefore the chemical composition of the interfacial region must include Fe and/or Ni. To determine the most probable AFM phase first principles calculations were carried out using projector augmented-wave pseudopotentials implemented by the Vienna *ab initio* simulation package (VASP).[45-49] In previous theoretical studies on the $NiTe_2$-1T phase, calculations using the functionals of LDA+U and PBE+U found distinctly different, non-magnetic solutions compared to those calculations employing hybrid functionals.[50] Therefore, the presence of correlation effects is important for elucidating the magnetic ground state of the $NiTe_2$-1T phase, which led to the choice of the SCAN functional as has been shown to be successful at incorporating correlation effects overlooked using the PBE or LDA (even without including the U parameter).[51-53] Here, an energy cutoff of 520 eV was used and the Brillouin zone was sampled by a Γ-centered grid with points evenly spaced at most 0.07/Å apart. The lattice parameters and atomic positions were relaxed with the conjugate gradient method until the forces in the unit cell were less than 0.008 eV/Å and self-consistency was reached when the energy difference between the electronic steps was less than 10^{-7} eV. Again, based on the STEM-EELS data there is Fe and Ni diffusion into the Sb_2Te_3 film, therefore the chemical composition in the interfacial AFM phase must be a combination of Ni, Fe, Sb, and/or Te. The interfacial crystal structure in the high resolution HAADF-STEM images closely resemble XY_2 – 1T phase (X= Ni, Fe and Y= Te, Sb), but we are not ruling out the XY_2 – 2H phase in our calculations. Additionally, we have included materials with space group 194 and atomic formula XY. We performed first principles calculations on the possible combinations of X and Y elements in these three structures (XY_2 – 1T, XY_2 – 2H, and XY). First, we tested for stable magnetic solutions with any magnetic moments on the unit cell equal to or larger than $0.01\mu_B$. Although we cannot make a direct comparison between our bulk calculations employing the SCAN functional with the aforementioned hybrid functional calculations of monolayers the total magnetic moments should be similar. We found moments of $2.04\mu_B$ and $0.08\mu_B$ for $FeTe_2$-2H and $NiTe_2$-1T respectively which is consistent with the $2.00\mu_B$ and $0.11\mu_B$ reported in Ref. 50.[50] These results are summarized in Table II.

TABLE II: Presence of stable magnetic solutions. The magnetic moments on the unit cells are given in units of μ_B

	Sb	Sb_2-1T	Sb_2-2H	Te	Te_2-1T	Te_2-2H
Fe	3.87	2.27	2.57	4.90	2.38	2.04
Ni	0.00	0.00	0.00	0.00	0.08	0.00

For materials identified to have stable magnetic solutions, we then performed supercell calculations using the lattice constants and atomic positions optimized in the primitive unit cell. For the XY structure there are two X-atomic sites in the primitive cell – thus, the out-of-plane (OP) AFM solution was calculated for the XY primitive cells. For the XY_2 structures a 1x1x2 super cell was used to calculate the energy of OP AFM solutions. For the XY, XY_2-1T, and XY_2-2H structures a 2x2x1 super cell was used to calculate the energy of the in-plane (IP) AFM solutions. Note, the three IP AFM arrangements that are possible in the 2x2x1 super cell are all equivalent due to the 3-fold symmetry, therefore we only record one solution. The energy differences between these equivalent states are less than 0.01 meV. If a given material's ground state is AFM, then the FM state must be higher in energy than the AFM state. In Table III the results are summarized with the recorded energy differences between the lowest energy state for each structure and formula with the IP and OP AFM, FM, and the non-magnetic (NM) states. While $NiTe_2$-1T phase was a possible candidate for the AFM interfacial phase based on the structural similarities identified in the HAADF-STEM images and previous reports of antiparallel moments between Ni and Te sites in literature,[50] the $NiTe_2$-1T phase showed no stable AFM solutions in our calculations. Specifically, when magnetic moments were initialized with antiparallel moments between the Ni-sites the final solution after self-consistency was always NM.

TABLE III: Ground state energies (eV/F.U.)

	IP AFM	OP AFM	FM	NM
FeSb	0.0000	0.1292	0.0986	0.4113
$FeSb_2$ - 1T	0.0643	0.0208	0.0000	0.5368
$FeSb_2$ - 2H	0.0138	0.0430	0.0000	0.3399
FeTe	0.0014	0.1116	0.0000	0.9172
$FeTe_2$ - 1T	0.0000	0.1119	0.0554	0.3068
$FeTe_2$ - 2H	0.1393	0.0105	0.0000	0.4586
$NiTe_2$ - 1T	unstable	unstable	0.0003	0.0000

Out of the candidate materials only the FeSb and $FeTe_2$-1T phase were found to have AFM ground states. Their ground state is characterized by an intraplanar "stripe" like AFM coupling and interplanar FM coupling – this is depicted in Figure 6. While there are no studies, to our knowledge, to compare our FeSb AFM results, there are calculations on the FM state available – the FM results between these are in qualitative agreement, however they have smaller magnetic moments due to the implementation of different functionals in the calculations.[54] While both the FeSb and $FeTe_2$-1T phase are AFM, we do not observe FeSb-type structures in our HAADF-STEM images, therefore we have determined that the AFM interfacial phase present at the Sb_2Te_3/Py interface is consistent with the $FeTe_2$-1T phase.

Conclusions

In conclusion we have studied the Sb_2Te_3/Py heterostructure and, with low temperature magnetometry, discovered a large exchange bias which indicates the presence of FM/AFM exchange coupling. The HAADF-STEM and EELS materials characterization revealed Fe and Ni diffusion into the Sb_2Te_3 film, yielding the secondary phase formation of a $NiTe_2$-1T type structural phase. From first-principles calculations performed for structures of XY, XY_2-1T, and XY_2-2H (X= Ni, Fe and Y= Te, Sb), we found that $NiTe_2$-1T had no stable AFM solutions, whereas FeSb and $FeTe_2$-1T phase are AFM. While there is theoretical support that FeSb and $FeTe_2$-1T are AFM, based on our HAADF-STEM results, there is strong justification that the interfacial phase at the Sb_2Te_3/Py interface is consistent with the $FeTe_2$-1T phase. We must note that the precise chemistry of the interfacial phase could not be determined, therefore it is possible that the $FeTe_2$-1T and/or an intermixed $(Fe_{1-x}Ni_x)Te_2$-1T phase is present at the interface contributing to the AFM/FM exchange coupling. From Figure 3(d) the derivative of the ZFC curve is a bit broad which may indicate the AFM phase transition is smeared out with temperature. We believe that along with $FeTe_2$-1T phase that there is likely the existence of some $(Fe_{1-x}Ni_x)Te_2$-1T phase and that this nickel incorporation into the structure will most certainly alter the phase transition temperature. It is also important to emphasize that we have performed calculation only on hexagonal structures, therefore we did not explicitly study the tetragonal phase of FeTe which is a known antiferromagnet.[55,56] While this tetragonal FeTe phase is not evident in our STEM images it cannot be completely

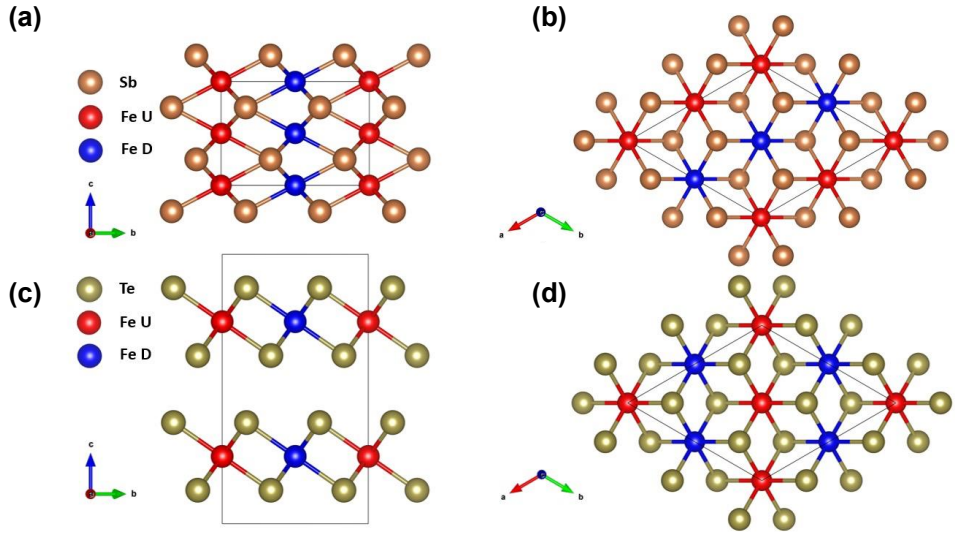

FIG 6. (a) The crystal structures of FeSb (a, b) and $FeTe_2$ -1T (c, d) are shown from along the *a*-lattice vector (a, c) and the *c*-lattice vector (b, d). The red and blue atoms represent spin up and spin down Fe atoms respectively, depicting the FM coupling between layers (a,c) and the "stripe" type AFM coupling (b,d) within layers.

ruled out here. It is possible $FeTe_2$-1T type phase is the prominent phase, but there could be traces of tetragonal FeTe that we could not explicitly identify here. Overall, this study has demonstrated that novel metastable phases may be formed at TI/FM interfaces, which should be the subject of further studies, because they may lead to the discovery of new magnetic and/or topological materials. Along with the discovery of the AFM interfacial material consistent with the intermixed (Fe,Ni)Te_2-1T phase, the interface was found to have significant disorder such as stacking faults and

an inhomogeneous interface. Additional, magnetic signatures of disorder were observed namely that the coercive field dependence and the exchange bias dependence are slightly different. We attribute the coercive field temperature dependence to the presence of a magnetically frustrated interface leading to pinned domains that will contribute to the total switching energy. It is not a reach to assume this, because from the STEM imaging we can conclude the interface is highly inhomogeneous and rough which may influence magnetic frustration near the interface. Despite the magnetically frustrated interface and the formation of the $FeTe_2$-1T type phase at the Sb_2Te_3/Py interface, we still found evidence of spin-pumping in this system (significant enhancement in Gilbert damping accompanied by decrease in effective magnetization in-plane). This highlights that despite these mixed interfaces, heterostructures can still be used in spin-orbit-torque memory applications. However, it may be useful to mitigate this mixed interface formation by introducing a spacer layer such as Ag, or Ti.[57-61] More studies should be conducted about whether the spin-pumping effect is enhanced by the presence of an additional AFM phases at the interface of TI/FM heterostructures. While this work focused on the FM/AFM exchange coupling between permalloy and the interfacial AFM phase formed at the interface with Sb_2Te_3 there has been other interesting research directions focused on AFM/TI coupled interactions in literature. These exotic interactions range from interfacial superconductivity (Bi_2Te_3/FeTe)[62] to AFM-induced magnetic proximity effect in TI with potential to exhibit quantum anomalous Hall effect.[63-65]

Acknowledgements

A.R. Will-Cole, N. Bhattacharjee, N.X. Sun, S. Patel, and S.H. Tolbert acknowledge financial support from NSF TANMS ERC under Award 1160504. A.R. Will-Cole was supported by the National Defense Science and Engineering Graduate Fellowship of the Office of Naval Research. J.L. Hart was supported by the Gordon and Betty Moore Foundation EPiOS Synthesis Investigator Award. This work was partially supported by the National Science Foundation grant DMR-1905662 and the Air Force Office of Scientific Research award FA9550-20-1-0247 (D. Heiman). Matthew Matzelle and Arun Bansil acknowledge support of the support of the US Department of Energy (DOE), Office of Science, Basic Energy Sciences Grant No. DE-SC0022216 (accurate modeling of complex magnetic states) and benefited from Northeastern University's Advanced Scientific Computation Center and the Discovery Cluster and the National Energy Research Scientific Computing Center through DOE Grant No. DE-AC02-05CH11231.

Conflicts of Interest

The authors do not have any conflicts of interest to declare.

References

1. A. Bansil, H. Lin, and T. Das, *Rev. Mod. Phys.*, **88**, 021004, (2016).
2. M.Z. Hasan and C.L. Kane, *Rev. Mod. Phys.*, **82**, 3045, (2010).
3. N.P. Armitage, E.J. Mele, and A. Vishwanath, **90**, 015001, (2018).
4. Y. Cao, G. Xing, H. Lin, H. Zheng, and K. Wang, *iScience*, **23**, 10, 101614, (2020).
5. A.R. Mellnik, J.S. Lee, A. Richardella, J.L. Grab, P.J. Mintum, M.H. Fisher, A. Vaezi, A. Manchon, E.-A. Kim, N. Samarth, and D.C. Ralph, *Nature*, **511**, 449 (2014).
6. M. DC, R. Grassi, J.Y. Chen, M. Jamali, D. Reifsnyder Hickey, D. Zhang, Z. Zhao, H. Li, P. Quarterman, Y. Lv *et al*, *Nature Mater*, **17**, 800-807 (2018).
7. N.H.D. Khang, Y. Ueda, and P.N. Hai, *Nature Mater.*, **17**, 808-813, (2018).
8. Q. Lu, P. Li, Z. Guo, G. Dong, B. Peng, X. Zha, T. Min, Z. Zhou, and M. Liu, *Nat. Commun.*, **13**, 1650, (2022).
9. M. Jamali, J.S. Lee, J.S. Jeong, F. Mahfouzi, Y. Lv, Z. Zhao, B.K. Nikolić, K. Andre Mkhoyan, N. Samarth, J.-P. Wang, *Nano Lett.*, **15**, 10, 7126-7132, (2015).
10. Y. Deng, M. Yang, Y. Ji, and K. Wang, *J. Magn. Magn. Mater.*,**496**, 165920, (2020).
11. Y. Tokura, K. Yasuda, and A. Tsukazaki, *Nat. Rev. Phys.*, **1**, 126-143, (2019).
12. A.J. Bestwick, E.J. Fox, X. Kou, L. Pan, K.L. Wang, and D. Goldhaber-Gordon, *Phys. Rev. Lett.*, **114**, 187201, (2015).
13. C.Z. Chang, W. Zhao, D. Kim, H. Zhang, B.A. Assaf, D. Heiman, S.-C. Zhang, C. Liu, M.H.W. Chan, J.S. Moodera, *Nature Mater.*, **14**, 473, (2015).
14. J.-M. Zhang, W. Zhu, Y. Zhang, D. Xiao, and Y. Tao, *Phys. Rev. Lett.*, **109**, 266405, (2012).

15. C. Liu, Y. Wang, M. Yang, J. Mao, H. Li, Y. Li, J. Li, H. Zhu, J. Wang, L. Li *et al*, *Nat. Commun.*, **12**, 4647, (2021).
16. K. He, *npj Quantum Mater.*, **5**, 90, (2020).
17. P. Wei, F. Katmis, A. Badih, A. Assaf, H. Steinberg, P. Jarillo-Herrero, D. Heiman, and J. S. Moodera, *Phys. Rev. Lett.*, **110**, 18680, (2013).
18. M. Lang, M. Montzeri, M.C. Onbasli, X. Kou, Y. Fan, P. Upadhyaya, K. Yao, F. Liu, Y. Jiang, W. Jiang *et al*, *Nano Lett.*, **14**, 6 3459, (2014).
19. F. Katmis, V. Lauter, F. Nogueira, B.A. Assaf, M.E. Jamer, P. Wei, B. Satpato, J.W. Freeland, I. Eremin, D. Heiman, P. Jarillo-Herrero, and J.S. Moodera, *Nature*, **533**, 513, (2016).
20. T. Liu, J. Kally, T. Pillsbury, C. Liu, H. Chang, J. Ding, Y. Cheng, M. Hilse, R. Engel-Herbert, A. Richardella, N. Samarth, and M. Wu, *Phys. Rev. Lett.*, **125**, 017204, (2020).
21. L.J. Riddiford, A.J. Grutter, T. Pillsbury, M. Stanley, D. Reifsnyder Hickey, P. Li, N. Alem, N. Samarth, and Y. Suzuki, *Phys. Rev. Lett*., **128**, 126802 (2022).
22. M.D. Davydova, A.S. Pakhomov, A.N. Kuz'michev, P.M. Vetoshko, P.N. Skirdkov, H.C. Han, Y.S. Chen, J.G. Lin, J.C. Wu, J.C.A. Huang, and K.A. Zvezdin, *J. Elect. Mater.*, **48**, 3, (2019).
23. A. Baker, A. Figueroa, L. Collins-McIntyre, G. van der Laan, and T. Hesjedal, *Sci. Rep.*, **5**, 7907, (2015).
24. C.D. Spataru and F. Leonard, *Phys. Rev. B*, **90**, 085115, (2014).
25. W. Ye, A.B. Pakhomov, S. Xu, H. Lu, Z. Wu, Y. Han, T. Han, Y. Wu, G. Long, J. Lin *et al*, *arXiv*, DOI: https://doi.org/10.48550/arXiv.1511.03421, (2015).
26. L.A. Walsh, C.M. Smyth, A.T. Barton, Q. Wang, Z. Che, R. Yue, J. Kim, M.J. Kim, R. M. Wallace, and C.L. Hinkle, *J. Phys. Chem. C.*, **121**, 42, (2017).
27. S.-J. Chang, P.-Y. Chuang, C.-W. Chong, Y.-J. Chen, J.C.-A. Huang, P.-W. Chen, and Y.-C. Tseng, *RSC Adv.*, **8**, 7785, (2018).
28. N. Bhattacharjee, K. Mahalingam, A. Fedorko, V. Lauter, M. Matzelle, B. Singh, A. Grutter, A.R. Will-Cole, M. Page, M. McConney, R. Markiewicz, A. Bansil, D. Heiman, and N.X. Sun, *Adv. Mater.*, **34**, 2108790, (2022).
29. M. Yan, H. Huang, K. Zhang, E. Wang, W. Yao, K. Deng, G. Wan, H. Zhang, M. Arita, H. Yang *et al*, *Nature Commun.*, **8**, 257, (2017).
30. C. Xu. B. Li, W. Jiao, W. Zhou, B. Qian, R. Sankar, N.D. Zhigadlo, Y. Qi, D. Qian, F.-C. Chou, and X. Xu, *Chem. Mater*., **30**, 14, (2018).
31. S. Chen, H. Liu, F. Chen, K. Zhou, and Y. Xue, *ACS Nano*, **14**, 9, 11473, (2020).
32. H. Wu, Z. Feng, A. Pal, H. Dong, C. Jing, K. Wang, S. Zhang, W. Deng, S. Li, J. Feng *et al*, *Chem. Mater*. **33**, 13, (2021).
33. A. Podpirka, J. Gagnon, C. Zgrabik, J. Pierce, and D. Shrekenhamer, *J. Vac. Sci. Technol. B*, **38**, 032210 (2020).
34. Supplemental Material
35. K. Hoefer, C. Becker, S. Wirth, and L.H. Tjeng, *AIP Advances*, **5**, 097139, (2015).
36. S. Mizukami, Y. Ando, and T. Miyazaki, *Jpn. J. Appl. Phys.*, **40**, 580, (2001).
37. M. Morota, Y. Saito, and N. Uchida, *Phys. Status Solidi RRL*, 2100247, (2021).
38. Y. Chen, X. Gu, Y. Li, X. Du, L. Yang, and Y. Chen, *Matter*, **3**, 1114, (2020).
39. C. Tang, Q. Song, C.-Z. Chang, Y. Xu, Y. Ohnuma, M. Matsuo, Y. Liu, W. Yuan, Y. Yao, J.S. Moodera, S. Maekawa, W. Han, and J. Shi, *Sci. Adv.*, **4**, eaas8660, (2018).
40. K. Kondou, R. Yoshimi, A. Tsukazaki, Y. Fukuma, J. Matsuno, K.S. Takahashi, M. Kawasaki, Y. Tokura, and Y. Otani, *Nature Phys.*, **12**, 1027, (2016).
41. J. Nogués and I.K. Schuller, *J. Magn. Magn. Mater.*, **192**, 2, 203, (1999).
42. J. Li, Y. Li, S. Du, Z. Wang, B.-L. Gu, S.-C. Zhang, K. He, W. Duan, and Y. Xu, Sci. Adv., 5, 6, (2019)
43. The Materials Project. Materials Data on $NiTe_2$ by Materials Project. United States. doi:https://doi.org/10.17188/1200993
44. E.J, Kirkland. Advanced computing in electron microscopy. New York: Plenum Press, (1998).
45. G. Kresse and D. Joubert, *Phys. Rev. B* **59**, 1758 (1999).
46. G. Kresse and J. Hafner, *Phys. Rev. B.*, **47**, 558 (1993).
47. G. Kresse and J. Hafner, *Phys. Rev. B.*, **49**, 14251 (1994).
48. G. Kresse and J. Furthmüller, *Comput. Mat. Sci*. **6**, 15 (1996).
49. G. Kresse and J. Furthmüller, *Phys. Rev. B*, **54**, 11169, (1996).
50. M. Aras, Ç. Kılıç, and S. Ciraci, *Phys. Rev. B*, **101**, 054429 (2020).
51. J. Sun, A. Ruzsinszky, and J. P. Perdew, *Phys. Rev. Lett*., **115**, 036402, (2015).
52. C. Lane, J.W. Furness, I.G. Buda, Y. Zhang, R.S. Markiewicz, B. Barbiellini, J. Sun, and A. Bansil, *Phys. Rev. B*, **98**, 125140, (2018).
53. J. Sun, R.C. Remsing, Y. Zhang, Z. Sun, A. Ruzsinszky, H. Peng, Z. Yang, A. Paul, U. Waghmare, X. Wu, M.L. Klein, and J.P. Perdew, *Nature Chem.*, **8**, 831, (2016).

54. A. Jain, S. P. Ong, G. Hautier, W. Chen, W. Davidson Richards, S. Dacek, S. Cholia, D. Gunter, D. Skinner, G. Ceder, and K.A. Persson, *APL Mater.*, **1**, 011002, (2013).
55. E.E. Rodriguez, C. Stock, P. Zajdel, K.L. Krycka, C.F. Majkrazak, P. Zavalij, and M.A. Green, *Phys. Rev. B.*, **84**, 064403, (2011).
56. C. Trainer, M. Songvilay, N. Qureshi, A. Stunault, C.M. Yim, E.E. Rodriguez, C. Heil, V. Tsurkan, M.A. Green, A. Loidl, P. Wahl, and C. Stock, *Phys. Rev. B.*, **103**, 024406, (2021).
57. V. Sharma, W. Wu, P. Bajracharya, D. Quang To, A. Johnson, A. Janotti, G.W. Bryant, L. Gundlach, M.B. Jungfleisch, and R.C. Budhani, *Phys. Rev. Mater.*, **5**, 124410, (2021).
58. N. Bhattacharjee, K. Mahalingam, A. Will-Cole, Y. Wei, A. Fedorko, C.T. Bowers, M. Page, M. McConney, D. Heiman, and N.X. Sun, *Adv. Mater. Interfaces*, **9**, 2201691, (2022).
59. F. Bonell, M. Goto, G. Sauthier, J.F. Sierra, A.I. Figueroa, M.V. Costache, S. Miwa, Y. Suzuki, and S.O. Valenzuela, *Nano Lett.*, **20**, 8, 5893, (2020).
60. H. Wu, P. Zhang, P. Deng, Q. Lan, Q. Pan, S.A. Razavi, X. Che, L. Huang, B. Dai, K. Wong, X. Han, and K.L. Wang, *Phys. Rev. Lett.*, **123**, 207205, (2019).
61. K. Kondou, R. Yoshimi, A. Tsukazaki, Y. Fukuma, J. Matsuno, K.S. Takahashi, M. Kawasaki, Y. Tokura, and Y. Otani, *Nat. Phys.*, **12**, 1027, (2016).
62. Q.L. He, H. Liu, M. He, Y.H. Lai, H. He, G. Wang, K.T. Law, R. Lortz, J. Wang and I.K. Sou, *Nat. Commun.*, **5**, 4247 (2014).
63. Q.L. He, X. Kou, A.J. Grutter, G. Yin, L. Pan, X. Che, Y. Liu, T. Nie, B. Zhang, S.M. Disseler *et al*, *Nat. Mater.*, **16**, 94, (2017).
64. Y. Liu, X. Niu, R. Zhang, Q. Zhang, J. Teng, and Y. Li, *Chinese Physics Letters*, **38**, 5 (2021).
65. P. Liu, C. Eckberg, L. Pan, P. Zhang, K.L. Wang, and G. Lüpke, *Sci. Rep.*, **12**, 12117 (2022).